Arabian Journal for Science and Engineering (2024) 49:16729–16741
https://doi.org/10.1007/s13369-024-09256-3

RESEARCH ARTICLE-ELECTRICAL ENGINEERING

Enhanced Gain Dual-Port Compact Printed Meandered Log-Periodic Monopole Array Antenna Design with Octagonal-Ring Shaped FSS for Broadband 28 GHz Applications

Seyfettin Sinan Gültekin[1] · **Mehmet Yerlikaya**[2]

Received: 22 February 2023 / Accepted: 3 June 2024 / Published online: 25 June 2024
© The Author(s) 2024

Abstract

In this article, we propose a microstrip-fed printed meandered log-periodic monopole array (PMLPMA), and its dual-port configuration incorporating an octagonal ring frequency selective surface (FSS) layer. The dual-port PMLPMA antenna system has a compact structure with a total dimension of 18.75 × 18.75 mm^2 and is designed to operate in the 5G n257 (28 GHz) band. The proposed PMLPMA radiator consists of five log-periodic monopole array elements, and the dual-port antenna system comprises two identical PMLPMAs placed vertically next to each other. Additionally, an octagonal ring-shaped single-layer FSS was implemented on the proposed antenna system to increase the gain across the operational band. Simulation results demonstrate that the dual-port PMLPMA antenna achieves a peak gain of about 3.5 dBi without the FSS layer, while a peak gain of 7.35 dBi is achieved when the FSS layer is augmented on the antenna. Moreover, isolation levels exceeding 30 dB are obtained for both cases between the 26.5–29.5 GHz frequency ranges. To verify the simulation results, the dual-port PMLPMA antenna system, and the octagonal ring-shaped FSS layer are also prototyped. The measurements align closely with the simulations in terms of performance criteria such as gain, bandwidth, and radiation patterns. Thus, the 28 GHz band antenna system exhibits great potential for 5G mobile applications.

Keywords 5G · mm-wave · Dual-port · Log-periodic · FSS

1 Introduction

Nowadays, mobile communication has taken its place as an indispensable part of our daily lives. Especially in the last decades, mobile communication has made tremendous progress with the growing demand for mobility, and its evolution from the first generation (1G) to the fifth generation (5G) represents a significant milestone in wireless communication [1]. As current wireless communication technologies primarily utilize sub-6 GHz bands, there is a pressing need for additional bandwidth and capacity to support the increasing data traffic. This has led to the exploration of more efficient utilization of the available spectrum, particularly at high frequencies such as millimeter-wave (mm-wave) [2]. Although mm-waves face challenges like high atmospheric absorption losses and production costs, several frequency bands for 5G mm-wave applications have been defined by ITU. These include the 24.25–27.5 GHz (n258), 26.5–29.5 GHz (n257), 27.5–28.35 GHz (n261), 37–40 GHz (n260), and 47.2–48.2 GHz (n262) bands [3]-23[4]. Among these bands, the n257 (28 GHz) band has gained significant attention in both industry and academia due to its lower atmospheric attenuation and global availability [1].

Printed antennas are particularly suitable for 5G mm-wave communication due to their benefits, such as ease of manufacturing, compact size, low cost, and compatibility with Monolithic Microwave Integrated Circuits (MMIC). However, these antennas also possess certain drawbacks, including narrow bandwidth and low gain [5]. In the case of mm-wave antennas, which require wide bandwidth, high gain, and efficiency, these limitations pose significant challenges due to factors such as high atmospheric absorption

✉ Mehmet Yerlikaya
mehmet.yerlikaya@selcuk.edu.tr

[1] Department of Electrical and Electronics Engineering, Engineering Faculty, Konya Technical University, 42100 Konya, Turkey

[2] Department of Airframe and Powerplant Maintenance, School of Civil Aviation, Selcuk University, 42250 Konya, Turkey

or limited radiant power capacity at high frequencies. Various methods have been proposed in the literature to address these issues, including the use of high relative permeability substrates, incorporation of slots or shorting pins, utilization of defected ground structures (DGS), addition of parasitic elements, adoption of frequency-independent antenna architectures like log-periodic structures, and using of metamaterial-based techniques such as superstrates, frequency selective surfaces (FSS), and electromagnetic band gaps (EBG) [5–19].

Furthermore, multi-port antenna technology has gained widespread adoption in mm-wave communication due to its ability to increase data transfer rates and ensure stable communication quality. The miniaturization of mobile devices necessitates the integration of multi-port antennas within a limited space. Designing multi-port antennas that maintain high isolation levels, low envelope correlation coefficients (ECC), and do not require decoupling structures is critical [20–23].

Over the past few years, there have been numerous advancements in the development of multi-port 5G antenna designs for the 28 GHz mm-wave [24–29]. For instance, one such design presented in [24] introduces a four-port MIMO antenna with T-shaped radiating elements. These T-shaped radiators are fed by coplanar waveguides (CPW), and split ring slots are incorporated into the defected ground planes. The proposed four-port MIMO antenna, etched on a Rogers RT-5880 substrate measuring 50.8 × 12 mm^2, offers a frequency bandwidth of 25.1–37.5 GHz and achieves a maximum gain of 10.6 dBi at 36 GHz. Another MIMO configuration described in [25] features a dielectric resonator antenna (DRA) with overall dimensions of 20 × 20 × 2.8 mm^3. This design covers a band of 0.85 GHz within the 27.5–28.35 GHz frequency range, providing a maximum isolation level of 24 dB and a peak gain of 8 dBi. In [26], a dual-port 2 × 8 MIMO antenna array with a substrate size of 23.6 × 55.1 mm^2 is proposed, offering an operating bandwidth of 27.49–29.42 GHz. This design achieves a peak gain of 11.33 dBi. Compact-sized MIMO antennas are also explored in [27] and [28], demonstrating good isolation levels and maximum gain values of 5.4 dBi and 5.9 dBi, respectively. Lastly, [29] proposes a four-port MIMO antenna with infinity shell-shaped patches featuring a substrate dimension of 30 × 30 mm^2. This design offers approximately 3.9 GHz bandwidth, an isolation level of 29 dB, and a peak gain of 6.1 dBi. These advancements in multi-port antenna designs highlight the ongoing efforts to optimize performance metrics such as bandwidth, isolation, and gain for 5G n257 band applications.

This paper proposes an improved dual-port PMLPMA (Printed Meandered Log-Periodic Monopole Array) antenna system for 28 GHz 5G mobile applications. The proposed antenna system is designed to achieve enhanced gain performance while maintaining a compact size. A novel octagonal-ring FSS layer is integrated into the antenna system to achieve gain improvement. The simulated results show that the dual-port antenna system with the FSS layer exhibits a bandwidth ranging from 26.5 to 29.5 GHz. The simulated and measured results demonstrate isolation levels exceeding 30 dB across the operational band. Moreover, the addition of the octagonal FSS layer results in a significant gain improvement of over 65% throughout the entire operating band of the antenna system. The proposed antenna system features a unique midpoint curved log-periodic architecture, distinguishing it from previous studies in the literature. This architecture not only provides the advantages of wideband performance associated with log-periodic patch antennas but also reduces the overall size of the antenna.

2 Design Procedures for the Dual-Port PMLPMA Antenna System

The geometry of the proposed PMLPMA and its dual-port configuration are presented in this part of the paper. Furthermore, parametric studies are also analyzed in this section. All the simulations are carried out by CST Studio Suite software.

2.1 Design Methodology of the Proposed PMLPMA

The proposed PMLPMA structure is inspired by conventional PLPDA (Printed Log-Periodic Dipole Array), as depicted in Fig. 1 [30]. The performance of the proposed PMLPMA, as in conventional PLPDA, is widely affected by various design parameters like spacing factor (σ), scale factor (τ), longest dipole length ($L_{\max}$), feed length (L_f), and number of dipole elements (N).

The design procedure for the proposed PMLPMA begins with determining the minimum and maximum cut-off frequencies (f_{min} and f_{max}) of the log-periodic array. Subsequently, the important design parameters of the dielectric constant or relative permittivity (ε_r) and substrate height (h_s) that impact the antenna radiation performance are identified. Then, effective relative permittivity (ε_{eff}) is obtained as follows:

$$\varepsilon_{eff} = \frac{\varepsilon_r + 1}{2} + \frac{\varepsilon_r - 1}{2} \frac{1}{\sqrt{1 + 12h_s/w}} \tag{1}$$

where the width of the microstrip-fed (w_f) is calculated as 1.55 mm by simultaneously solving Eqs. (1) and (2).

$$Z_c = \frac{120\pi}{\sqrt{\varepsilon_{eff}}\left[\frac{w}{h_s} + 1.393 + \frac{2}{3}\ln\left(\frac{w}{h_s} + 1.444\right)\right]} \tag{2}$$

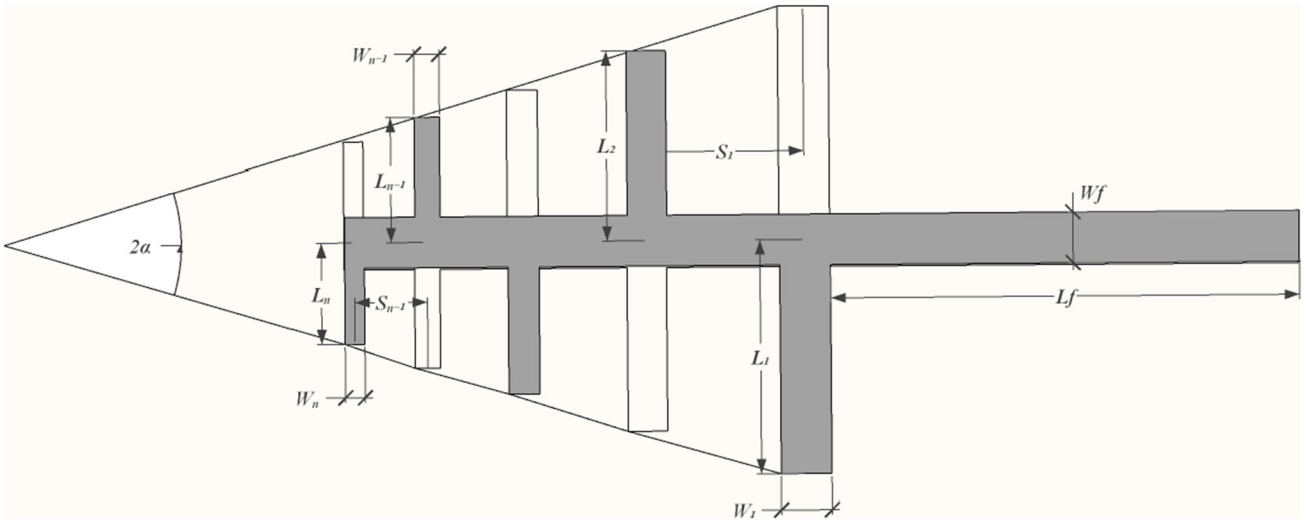


Fig. 1 Basic PLPDA architecture

Here Z_c represents the microstrip line's characteristic impedance, typically assumed to be 50 Ω, which corresponds to the impedance of the standard SMA connector. Thereafter, the length of the feed line (L_f) is calculated as 3.9 mm by Eq. (3);

$$L_f = \frac{c}{2f_0\sqrt{\varepsilon_{eff}}} \tag{3}$$

where c denotes the speed of light in free space. The resonant frequency of the antenna (f_0) is set to 28 GHz for this study. Afterward, the length of the longest log-periodic element (L_{max}) is determined to be approximately 2.07 mm using Eq. (4).

$$L_{\max} = L_1 = \frac{\lambda_{\max}}{4\sqrt{\varepsilon_{eff}}} = \frac{c}{4f_{\min}\sqrt{\varepsilon_{eff}}} \tag{4}$$

Then, the log-periodic antenna input parameters τ and σ need to be established. Equation (5) is used to calculate the space (S_n) between sequential array elements using the length of the nth element (L_n) and the space factor (σ).

$$\sigma = \frac{s_n}{4L_n} \tag{5}$$

The lengths of the log-periodic array elements are computed based on the scale factor (τ) using Eq. (6).

$$\tau = \frac{L_{n+1}}{L_n} = \frac{w_{n+1}}{w_n} = \frac{s_{n+1}}{s_n} \tag{6}$$

The total number of log-periodic elements (N) can be determined by Eq. (7).

$$N = 1 + \frac{\log(B.B_{ar})}{\log(1/\tau)} \tag{7}$$

where B_{ar} and B are the active region bandwidth and expected bandwidth of the log-periodic array, respectively. B_{ar} and B are obtained from Eqs. (8) and (9), while the half-aperture angle of the log-periodic array (α) is calculated using Eq. (10).

$$B_{ar} = 1.1 + 7.7(1-\tau)^2 \cot\alpha \tag{8}$$

$$B = \frac{f_{\min}}{f_{\max}} \tag{9}$$

$$\alpha = \tan^{-1}\left(\frac{1-\tau}{4\sigma}\right) \tag{10}$$

From the aforementioned equations, τ is optimized as 0.78, and the accompanying spacing factor (σ) is set as 0.17 for the proposed PMLPMA Furthermore, the parameters α and N are calculated as 35.8° and 5, respectively.

2.2 PMLPMA Geometry

Figure 2 shows 2D geometric views of the unit PMLPMA, while Table 1 provides the detailed dimensions of the PMLPMA. The proposed PMLPMA is designed to operate at 28 GHz band with a compact size of 4.15 × 13 mm^2. The proposed PMLPMA design is implemented on a double-sided Rogers RT-5880 dielectric laminate with a relative permittivity (ε_r) of 2.2 and a substrate height (h_s) of 0.508 mm. Unlike conventional PLPDAs, the proposed PMLPMA distinguishes itself through its unique structure, employing monopole elements that resemble mid-point bent radiator elements. The radiator of the PMLPMA consists of five meandered log-periodic monopole elements, and it is fed by a 50 Ω microstrip line. Additionally, there is a thin impedance matching line between the PMLPMA patch and

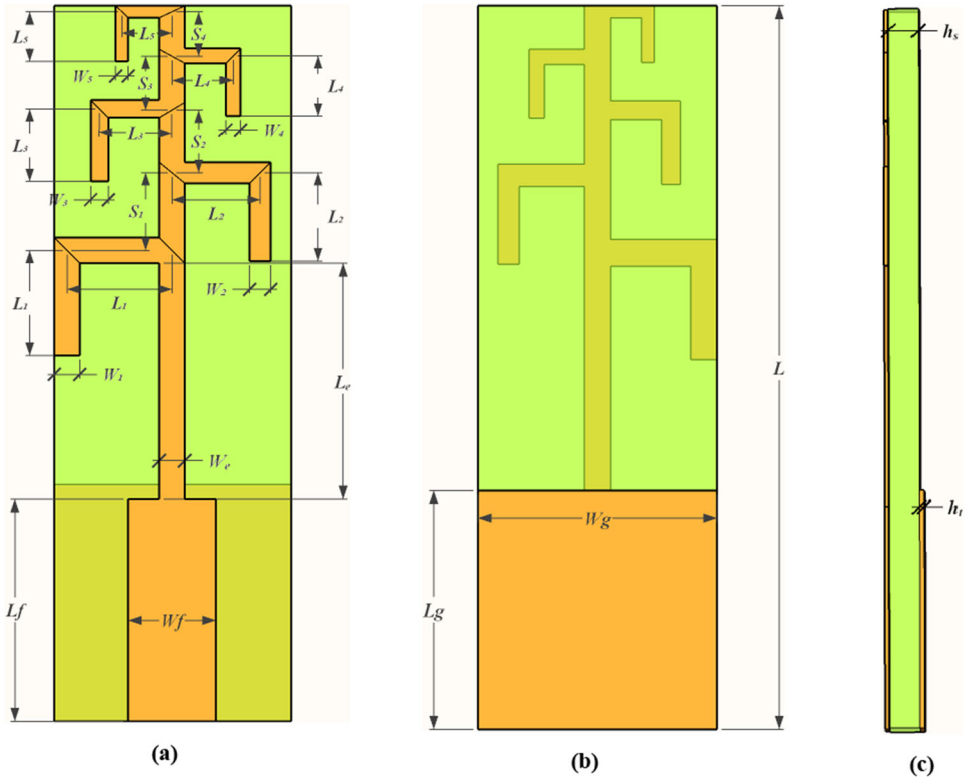


Fig. 2 Proposed PMLPMA geometry **a** top view **b** bottom view **c** side view

Table 1 The detailed dimensions of the unit PMLPMA structure (in mm)

L_e	L_f	L_g	L_1	L_2	L_3	L_4	L_5
4.15	3.9	4.15	2.07	1.6	1.25	0.975	0.76
W_e	W_f	W_g	W_1	W_2	W_3	W_4	W_5
0.45	1.55	4.15	0.45	0.35	0.275	0.225	0.175
S_1	S_2	S_3	S_4	L	h_s	h_t	
1.4	1.1	0.85	0.65	13	0.508	0.0035	

the microstrip feed line. On the backside of the laminate, a square ground plane with a side length of 4.15 mm is positioned to serve its purpose.

2.3 Dual-Port PMLPMA antenna

The proposed dual-port antenna system consists of two PMLPMA elements positioned orthogonally to each other, as illustrated in Fig. 3. The dual-port configuration of the PMLPMA antenna exhibits a highly compact structure, with dimensions of 18.75 × 18.75 mm^2. Figure 4 presents a comparison of the scattering parameters (s-parameters) between the individual unit PMLPMA and its dual-port configuration. The simulation results demonstrate that both the unit PMLPMA and its dual-port configuration exhibit similar return loss (S_{11}) characteristics. As observed in Fig. 4, the − 10 dB bandwidth of the dual-port PMLPMA spans from 26.6 to 30.1 GHz, while the unit PMLPMA antenna operates within a bandwidth ranging from 26.55 to 29.5 GHz.

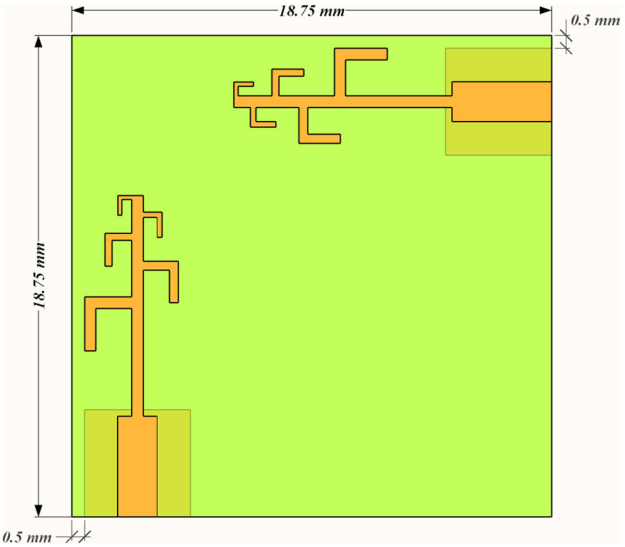


Fig. 3 2D architecture of the dual-port PMLPMA antenna

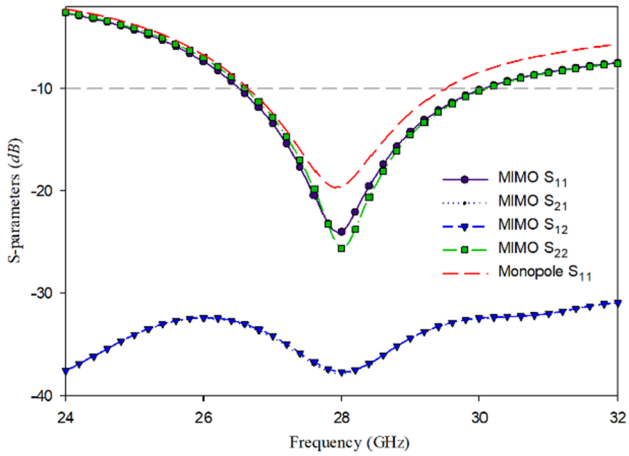


Fig. 4 Comparative s-parameters of the PMLPMA and its dual-port configuration

It is seen that both cases closely align with the target n257 band. Additionally, the proposed antenna achieves an isolation level exceeding 30 dB between the PMLPMA elements. Consequently, there is no requirement for any decoupling structure to mitigate the effects of mutual coupling.

To see the mutual coupling between the proposed dual-port antenna, surface current distributions were investigated separately for both ports at 28 GHz frequency using CST software, as shown in Fig. 5. While examining the current distribution, one port was excited and the other port was terminated with 50 Ω. It can be noticed that a small amount of current is generated in the terminated antenna as shown in the figure.

3 Octagonal Ring FSS

One of the key steps in eliminating path losses is to enhance the antenna gain. A significant technique for improving gain involves incorporating metamaterial-based layers like EBG, superstrate, or FSS. Figure 6 illustrates the setup of the antenna coupled with an FSS layer. In the figure, h_{ss} and d correspond to the height of the superstrate layer and the gap between the two substrates, respectively. To optimize the antenna gain, it is recommended that these two variables be approximately one-fourth of the wavelength [31].

The CST Studio Suite optimization tool was utilized to optimize the h_{ss} and d parameters for achieving a resonant frequency of 28 GHz. The resulting optimized values were 2.7 mm for h_{ss} and 1.55 mm for d. Figure 7 illustrates the proposed configuration of the octagonal ring FSS unit cell and its periodic structure. The unit cell is composed of two identical square rings that are interconnected perpendicular to each other. For the design of the unit FSS cell, Rogers RO3003 laminate was used, with a relative permittivity of 3, a height of 1.52, and a tangent loss of 0.0012.

The substrate length of the unit FSS cell (w_{sub}) was determined to be 3.75 mm using the equation given in Eq. (11). Through optimization, the conductor length of the FSS patch (L_p) and the width of the octagonal ring (w_p) were set to 3.5 and 0.1 mm, respectively. By referring to the figure, the spacing (s) between the FSS patch and the substrate edge was found to be 0.125 mm.

$$W_{sub} = \frac{c}{2f_0\sqrt{\frac{\varepsilon_r+1}{2}}} \tag{11}$$

The proposed octagonal ring FSS has been analyzed with simulations in terms of transmission coefficient (S_{21}) and reflection coefficient (S_{11}) according to variation of the incidence angle (θ). Figure 8 depicts the incidence angular characteristics of the octagonal ring FSS, considering both the *TE* and *TM* planes. It can be observed from the graphs that when $\theta = 0°$, S21 remains below $-$ 10 dB within the 25.4–30.7 GHz range, with the resonance frequency occurring at 28 GHz. The graphs indicate a slight shift in the resonant frequency for different theta angles in both planes.

Following the FSS design process, simulations were made for the dual-port PMLPMA antenna both with and without the FSS. The obtained peak gain and total efficiency results are compared in Fig. 8. After the FSS design process, performance analyses of the proposed antenna system were made for both with/without FSS cases. Comparative plots of the peak gain, total efficiency, and s-parameters for the proposed antenna are presented in Fig. 9.

As seen in Fig. 9a, the addition of a single layer FSS on top of the proposed dual-port PMLPMA antenna resulted in a notable increase in the maximum gain, rising from 3.5 dBi to approximately 7.35 dBi. Moreover, the dual-port antenna with FSS exhibited an overall efficiency improvement of approximately 5%. Gain-enhancing elements must have minimal impact on the operating band while increasing antenna performance. Therefore, the impact of the proposed octagonal-shaped FSS layer on the s-parameters of the antenna system was investigated and compared. The analysis revealed that in Fig. 9b, the proposed antenna with FSS exhibited an impedance bandwidth of 26.15–29.65 GHz, with a resonance frequency of 28.25 GHz. It can be concluded that the addition of FSS did not significantly alter the impedance bandwidth of the dual-port PMLPMA antenna. Only a slight shift in the resonant frequency was observed. Similarly, there is a slight difference in the isolation level between the antenna elements.

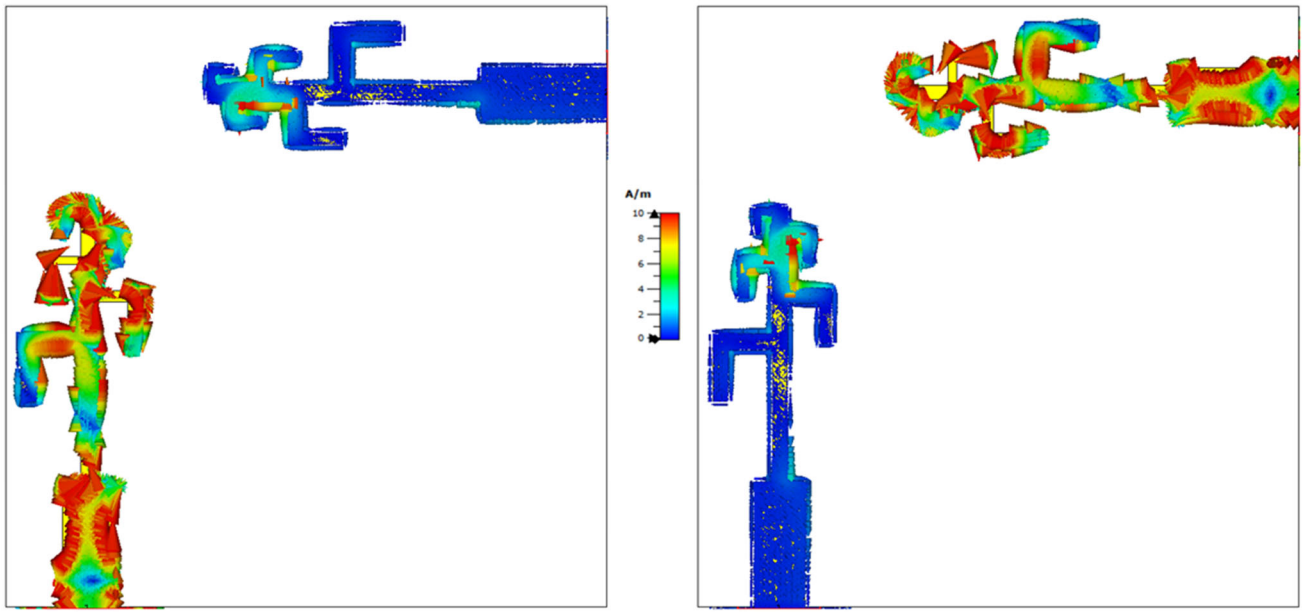


Fig. 5 The simulated surface current distributions of the dual-port PMLPMA antenna

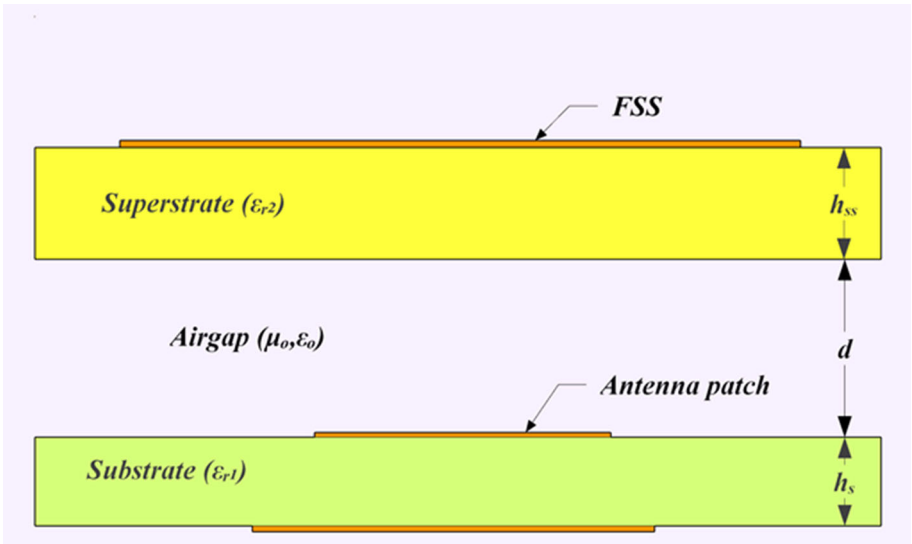


Fig. 6 Side view of an antenna with an FSS layer

4 Parametric Studies

The parametric analysis of the dual-port PMLPMA antenna began with an investigation into the design parameters of the unit PMLPMA antenna (Fig. 10). In Fig. 10a, the impact of the ground plane width (W_g) and length (L_g) on the operating band and resonance frequency of the unit PMLPMA antenna is investigated. The graphs reveal that increasing L_g from 3.9 to 4.4 mm results in an expansion of the antenna bandwidth and an increase in return loss while shifting the resonance frequency towards a higher frequency. Conversely, as the W_g parameter increases, the resonance frequency decreases while the return loss value increases. Similarly, Fig. 10b illustrates the variation of the proposed PMLPMA bandwidth through varying matching line width (W_e) and length (L_e). The figure demonstrates that enlarging both L_e and W_e dimensions has a lowering effect on the resonance frequency. Furthermore, it is observed that the return loss reaches its maximum level when L_e and W_e are set to 4.15 mm and 0.45 mm, respectively.

Additionally, the effects of the length of the unit FSS patch (L_p) and width of the FSS ring (w_p) on the FSS transmission loss are also studied, as shown in Fig. 11. The variations in L_p size impact both the resonant frequency and the operating bandwidth of the unit FSS cell. Increasing the L_p from 3.3 to 3.7 mm led to a decrease in the resonant frequency from 30.3

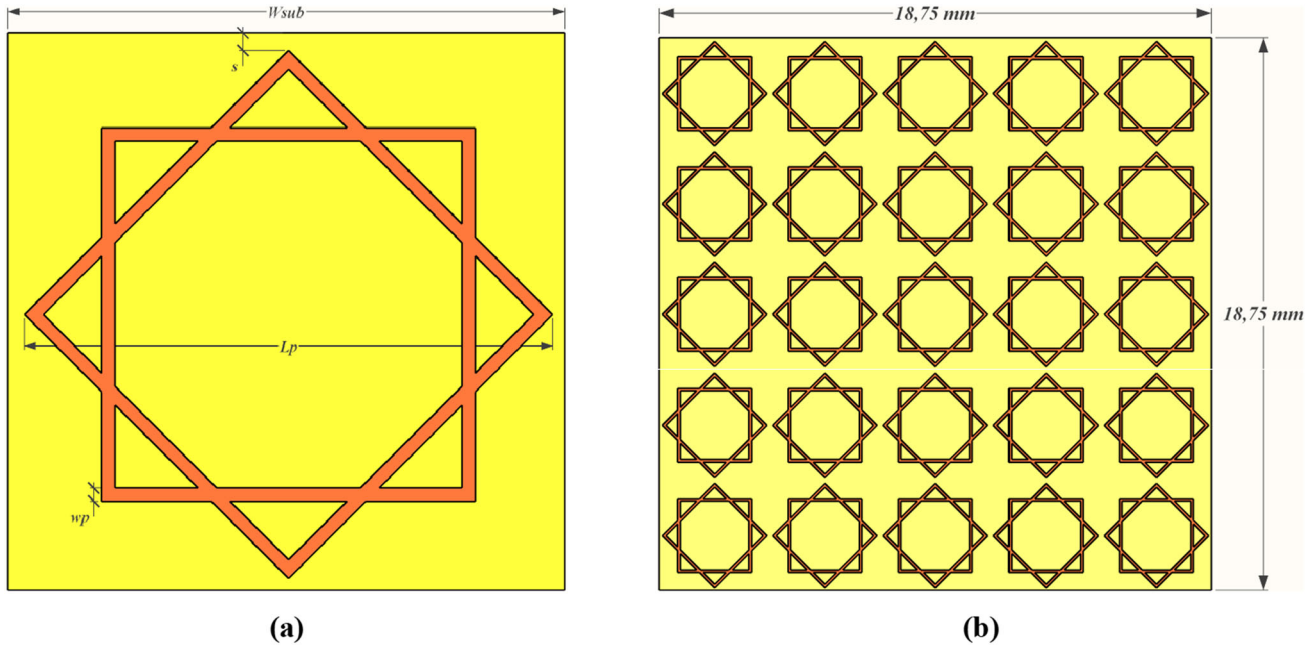


Fig. 7 The octagonal ring FSS **a** unit cell geometry **b** periodic structure

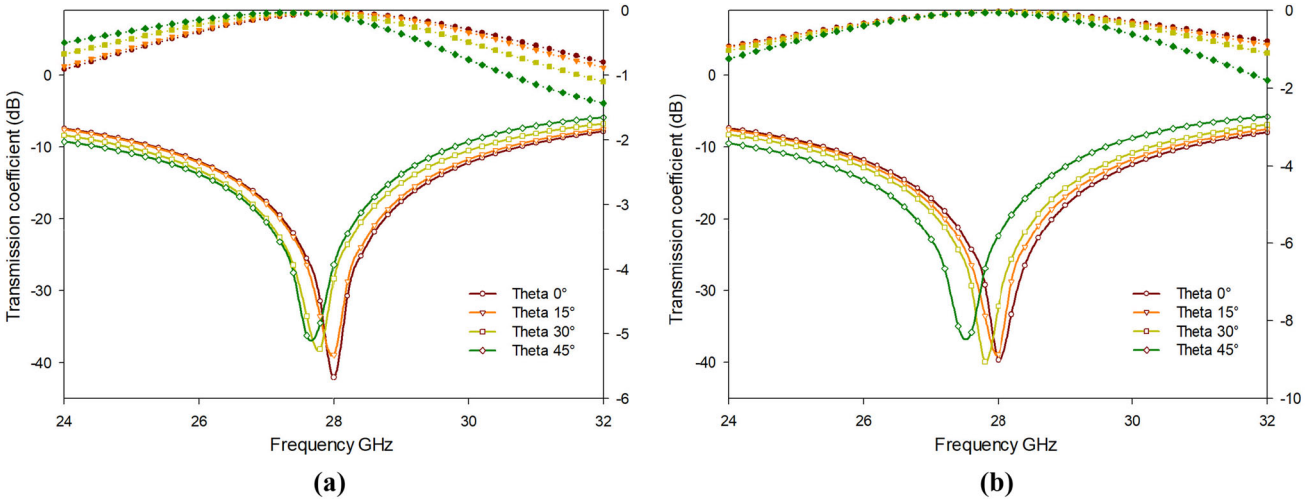


Fig. 8 Transmission (S_{21}) and reflection (S_{11}) coefficients of the proposed FSS at various theta (θ) angles for: **a** TE plane **b** TM plane

to 25.6 GHz. Similarly, adjusting the size of the w_p resulted in a comparable effect on the bandwidth and resonant frequency of the FSS. Increasing the w_p caused the resonant frequency of the FSS to shift from 27.5 to 28.5 GHz.

5 Results and Discussion

The dual-port PMLPMA antenna and octagonal ring FSS prototypes were fabricated on dielectric substrates of RT-5880 and RO3003, respectively. The dimensions of the substrates were 18.75 × 18.75 mm^2, as shown in Fig. 12.

Following the fabrication process, performance measurements of the proposed MIMO antenna were made in a semi-anechoic chamber utilizing a Keysight PNA-X 5244B vector network analyzer and an EBTRO EAMS-120 turntable. The measurement setup inside the semi-anechoic chamber is given in Fig. 13. This setup is crucial for reliable measurements of the proposed antenna system's performance.

Figure 14 shows the comparative s-parameter graphs for measured and simulated results of the proposed dual-port PMLPMA antenna with and without the octagonal ring FSS. The dual-port PMLPMA antenna without FSS is measured in the frequency range of 26.85 to 29.4 GHz, while the operating band of the antenna without FSS is measured as

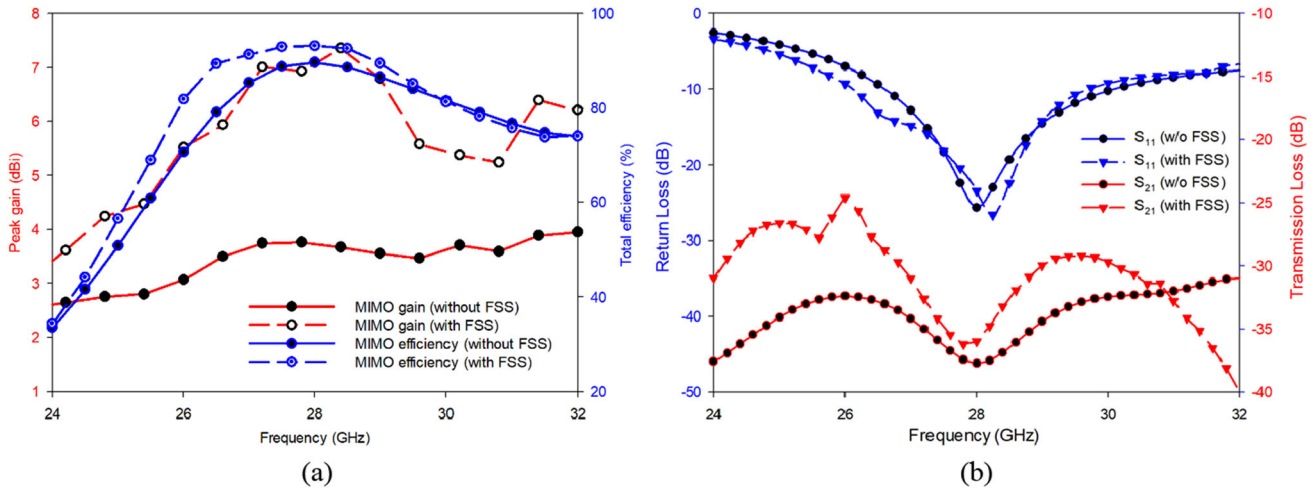


Fig. 9 Comparative performance plots of the dual-port PMLPMA antenna system with/without the octagonal ring FSS: **a** peak gain and total efficiency **b** s-parameters

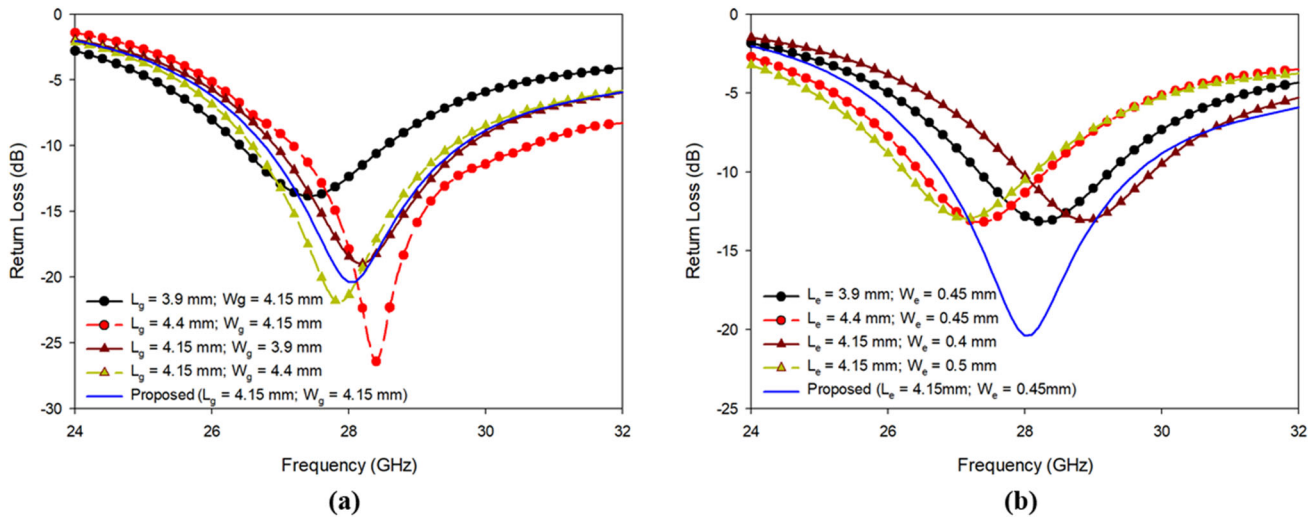


Fig. 10 Effects of some design parameters on the return loss of the proposed PMLPMA **a** L_g and W_g **b** L_e and W_e

26.65–29.75 GHz (Fig. 14a). The resonance frequencies for the antenna with and without FSS were also measured at 28.2 GHz and 27.7 GHz, respectively. Compared to the simulated results, the bandwidths of both the antenna system with and without FSS are largely similar, with a slight change in resonant frequencies. In addition, when the transmission coefficient (S_{21}) curves were examined, it was determined that the measured results are much better than the simulated ones. Therefore, although there are some differences in terms of resonance frequency and operating bandwidth, the simulation and measurement results of the proposed antenna largely overlap with the determined design values and cover almost the entire 5G n257 band.

Finally, the radiation pattern performance evaluations of the dual-port antenna are examined. In Fig. 15, we compare the measured and simulated polar radiation patterns of the proposed antenna, both with and without FSS, at a frequency of 28 GHz. Figure 15a presents the E-plane (*xz*-plane) pattern, while Fig. 15b depicts the H-plane (*yz*-plane) pattern of the antenna. The polar axis, spanning from 0° to 360°, represents the azimuth axis, defining angles in a circular pattern around the antenna. On the axis perpendicular to the polar axis, we observe the gain values corresponding to the azimuth angle.

As can be seen from the figure, the radiation patterns of both dual-port antenna with and without FSS were quite similar to each other. At the 28 GHz frequency point, the maximum gain values for the dual-port PMLPMA antenna with FSS were measured as 6.8 dBi in the xz-plane and 5.95 dBi in the yz-plane. In contrast, the maximum gains measured in the antenna without FSS were 3.1 dBi and 2.1 dBi in the E and H planes, respectively.

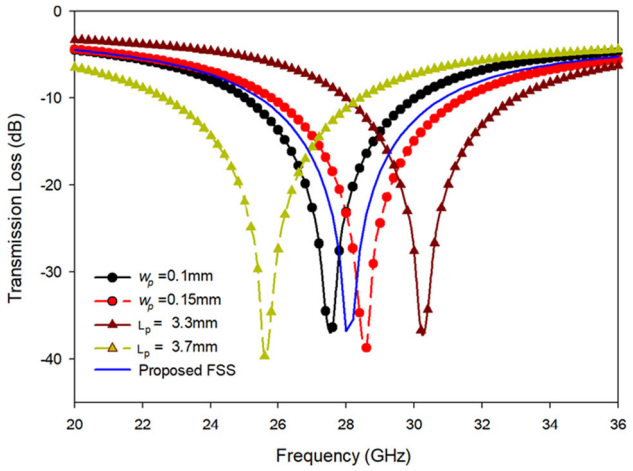


Fig. 11 Effects of the w_p and L_p parameters on the transmission loss of the proposed FSS

5.1 The Dual-Port PMLPMA Antenna's Diversity Performance

The diversity capability of the proposed antenna is verified through the examination of several performance attributes, namely the envelope correlation coefficient (ECC), diversity gain (DG), total active reflection coefficient (TARC), and channel capacity loss (CCL) [21].

ECC is a crucial parameter that quantifies the correlation level between multiple ports within an antenna system. In an ideal scenario, the ECC value should be precisely zero, indicating complete independence and isolation between the ports. However, in practical situations, an ECC value of less than 0.05 is considered adequate to achieve the best antenna performance. The ECC, denoted by the symbol ρ_e, can be computed using Eq. (12) by employing the radiation pattern of the antenna elements, as detailed in reference [20]. This measurement allows for a comprehensive assessment of the antenna's diversity capability, which is vital for enhancing its overall performance in wireless communication systems.

$$\rho_e = \frac{\left|\iint_{4\pi}\left[\overrightarrow{F_1}(\theta,\phi) * \overrightarrow{F_2}(\theta,\phi)\right]d\Omega\right|^2}{\iint_{4\pi}\left|\overrightarrow{F_1}(\theta,\phi)\right|^2 d\Omega \iint_{4\pi}\left|\overrightarrow{F_2}(\theta,\phi)\right|^2 d\Omega} \tag{12}$$

In the computation of ECC, several parameters come into play. The symbol Ω represents the solid angle, while the * denotes the Hermitian product operator. $F_i(\theta,\phi)$ displays the antenna's 3D field radiation pattern of the antenna when the *ith* port is activated. The ECC can also be determined using S-parameters, as illustrated in Eq. (13).

$$\rho_e = \frac{\left|S_{11}^* S_{12} + S_{21}^* S_{22}\right|^2}{\left(1 - |S_{11}|^2 - |S_{21}|^2\right)\left(1 - |S_{22}|^2 - |S_{12}|^2\right)} \tag{13}$$

The calculation of ECC involves complex mathematical operations and the examination of the antenna's radiation patterns and S-parameters. This comprehensive analysis helps in understanding the level of correlation between different ports in the antenna system, which in turn plays a critical role in optimizing the antenna's diversity capability and overall performance in practical wireless communication applications.

The received signals are combined using some diversity techniques to increase the signal-to-noise ratio (SNR) by using multiple antennas instead of a single antenna element.

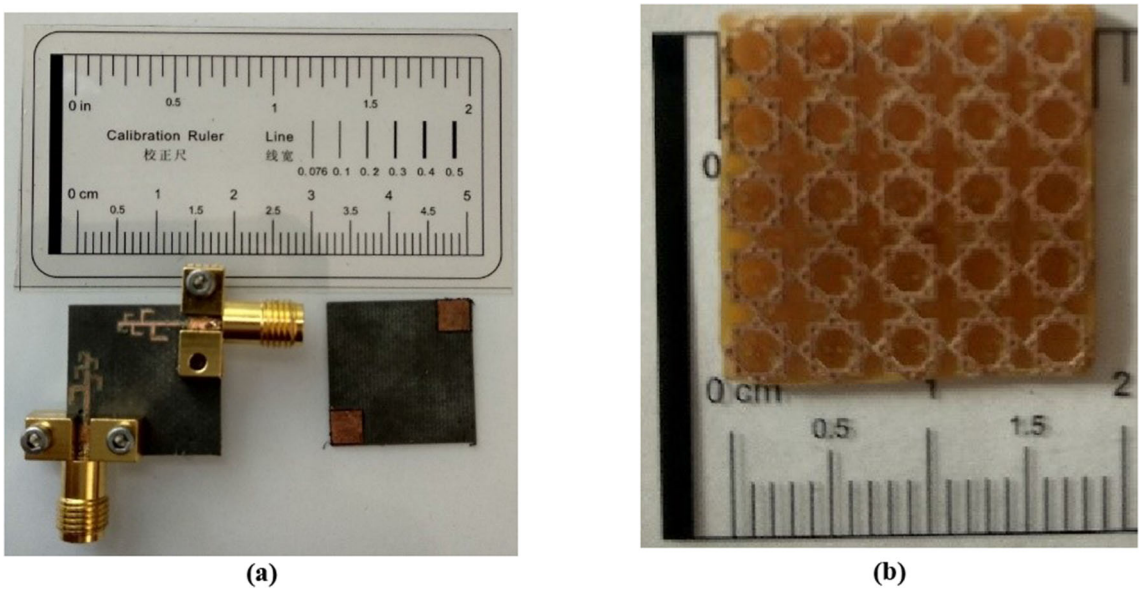


Fig. 12 Photographs of prototyped elements: **a** PMLPMA MIMO antenna **b** octagonal ring FSS

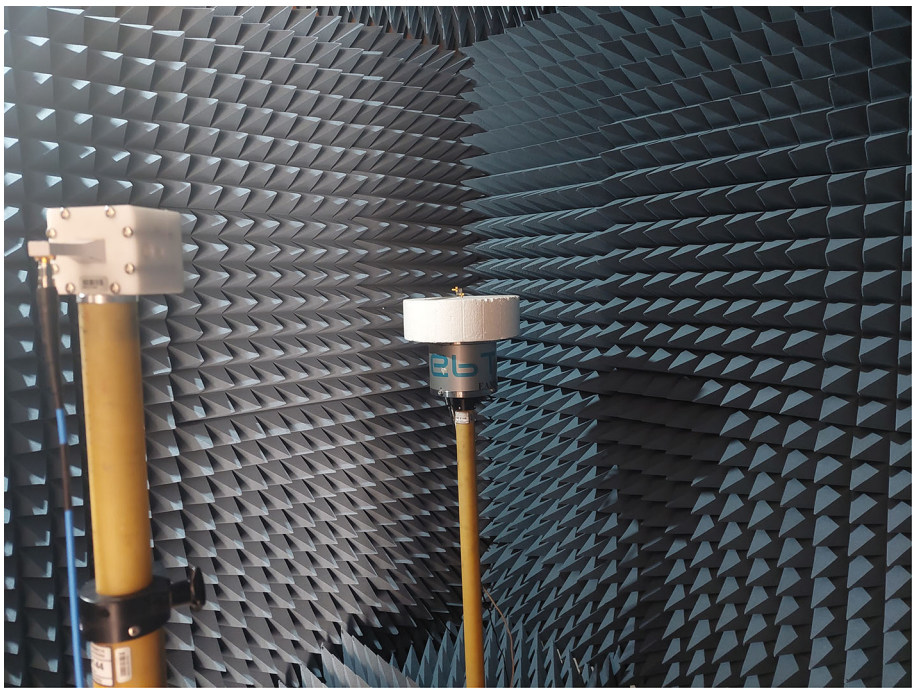


Fig. 13 Experimental setup for antenna measurement

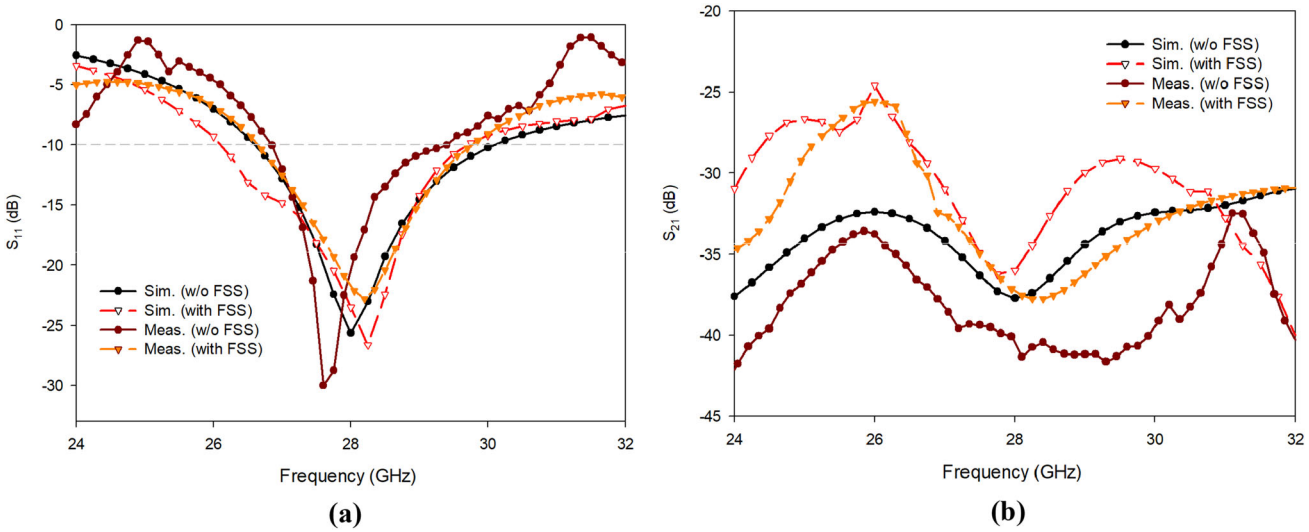


Fig. 14 Measured and simulated s-parameters of the dual-port PMLPMA antenna: **a** S_{11} **b** S_{21}

The diversity gain (DG) plays a significant role in characterizing this variation and is closely related to the correlation parameter ρ_e, as depicted in Eq. (14). The diversity gain provides valuable insights into the effectiveness of these techniques in mitigating signal fading and enhancing the overall communication performance.

$$DG = 10\sqrt{1 - (\rho_e)^2} \tag{14}$$

In Fig. 16a, a comparison between the measured and simulated ECC and DG curves of the dual-port PMLPMA antenna with an octagonal ring FSS layer is presented. The results show that the proposed dual-port PMLPMA antenna system exhibits a correlation well below 0.5, which meets the practical standard for ECC. Similarly, the DG remains stable at approximately 10 dB across the n257 band, indicating strong diversity performance of the antenna.

The scattering parameters (s-parameters) are insufficient to characterize the efficiency and bandwidth (BW) of the proposed antenna system. The total active reflection coefficient (TARC) is used to better characterize the multi-port antenna system. The TARC can be calculated using the s-parameters of the antenna as given in Eq. (15). In a multi-port antenna system, it is desirable to be less than − 10 dB TARC value

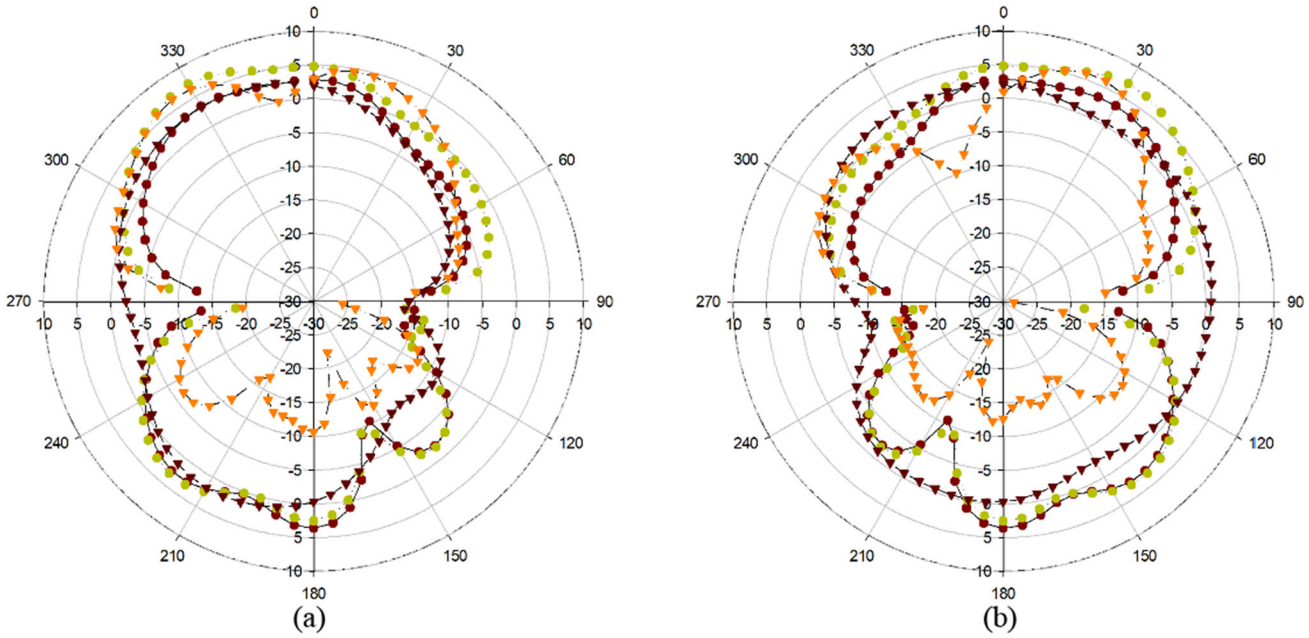


Fig. 15 Comparative radiation patterns of the dual-port PMLPMA antenna at 28 GHz **a** xz-plane; **b** yz-plane

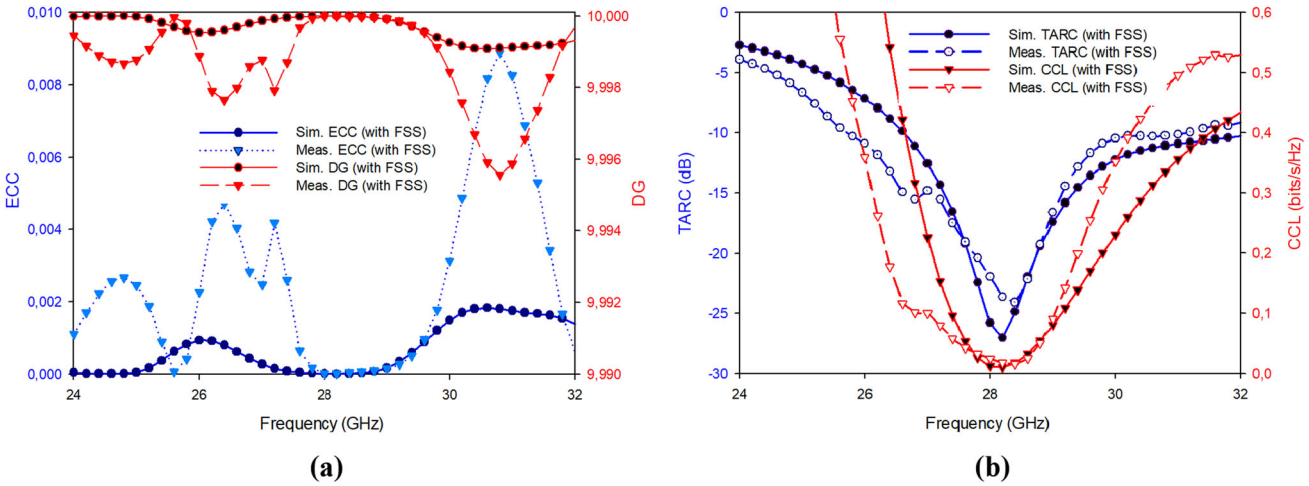


Fig. 16 Compared diversity characteristics of the proposed PMLPMA antenna system with FSS. **a** ECCvsDG; **b** TARCvsCCL

over the operating band for a good diversity performance.

$$TARC = \sqrt{\frac{\left(S_{ii} + S_{ij}\right)^2 + \left(S_{ji} + S_{jj}\right)^2}{2}} \tag{15}$$

Channel capacity loss (CCL) is another key metric of diversity performance in multi-port antennas, and it indicates the maximum data rate at which transmission can continue with little loss. CCL can also be calculated using the s-parameters of the antenna. Equation (16) gives the formula for CCL. In a multi-port antenna system, the maximum allowed CCL value is less than 0.4 bits/s/Hz.

$$CCL = -\log_2\left\{\det(\psi^R)\right\} \tag{16}$$

where ψ^R is the correlation matrix found by the equations given below.

$$\psi^R = \begin{bmatrix} \sigma_{11} & \sigma_{12} \\ \sigma_{21} & \sigma_{22} \end{bmatrix} \tag{17}$$

$$\sigma_{ii} = 1 - \left(|S_{ii}|^2 - |S_{ij}|^2\right) \tag{18}$$

$$\sigma_{ij} = -\left(S_{ii} * S_{ij} + S_{ji} S_{ii}*\right) \tag{19}$$

Table 2 Comparison of the dual-port PMLPMA antenna with related 28 GHz antennas

Ref.	antenna size (in mm^2)	Number of ports	BW (GHz)	Peak gain (dBi)	İsolation (dB)	ECC (dB)
[25]	400	2	0.85	8	24	0.013
[26]	1300.4	2	1.95	10.3	40	–
[27]	450	2	6.4	5.4	35	0.005
[28]	375	2	3.9	5.9	30	0.16
This study	351.5	2	3	7.2	33	0.004

Figure 16b shows the TARC and CCL performances of the dual-port PMLPMA antenna. The graphs show that both the measured and simulated TARC values are consistently below − 10 dB throughout the operating band. Likewise, the graphs demonstrate that the CCL value is substantially lower than the threshold value, which indicates that the proposed antenna system is viable for 28 GHz 5G applications.

5.2 Comparison with Related Studies

Table 2 compares the proposed PMLPMA antenna system's performance parameters with the state-of-the-art 28 GHz dual-port antennas presented in [25–28]. Based on the data in the table, it is clear that the proposed antenna is the most compact in size and has the best ECC level. It also seems that the isolation level between antenna ports is one of the best. Although the designs given in [25, 26] have higher peak gain, the proposed dual-port antenna is also quite good in terms of peak gain compared to the others. Finally, the proposed antenna system has a simplier and less costly design configuration.

6 Conclusion

This article presents a novel log-periodic dual-port antenna system for 28 GHz 5G communication systems. The proposed dual-port antenna configuration consists of two identical PMLPMAs and each PMLPMA consists of 5 innovative mid-curved radiating log-periodic elements. In addition, a new octagonal ring-shaped FSS layer is used on the dual-port PMLPMA antenna to achieve high gain, and a detailed analysis of the FSS is also presented. The proposed antenna system demonstrates a simulated bandwidth ranging from 26.5 to 29.5 GHz. Measurements were also performed in a semi-anechoic chamber to validate the antenna performance, and the results closely align with the simulations, indicating the accuracy of the proposed design. The isolation levels between the ports were found to be less than − 30 dB in both simulated and measured results, ensuring good isolation and reduced interference. Moreover, the measured peak gain of the proposed antenna exhibited a notable improvement from 3 to 6.8 dBi, while the simulated peak gain increased from 3.5 to 7.35 dBi. Remarkably, the gain was enhanced by over 65% across the entire operating band, signifying the significant gain improvement achieved through the proposed design. These results validate the effectiveness of the novel log-periodic dual-port antenna, making it a promising candidate for 5G communication systems operating at 28 GHz frequencies.

Acknowledgements This study was supported by Konya Technical University Scientific Research Fund (BAP) with grant number of 201102049.

Funding Open access funding provided by the Scientific and Technological Research Council of Türkiye (TÜBİTAK).

Declarations

Conflict of interest The authors have no conflicts of interest to declare.

Open Access This article is licensed under a Creative Commons Attribution 4.0 International License, which permits use, sharing, adaptation, distribution and reproduction in any medium or format, as long as you give appropriate credit to the original author(s) and the source, provide a link to the Creative Commons licence, and indicate if changes were made. The images or other third party material in this article are included in the article's Creative Commons licence, unless indicated otherwise in a credit line to the material. If material is not included in the article's Creative Commons licence and your intended use is not permitted by statutory regulation or exceeds the permitted use, you will need to obtain permission directly from the copyright holder. To view a copy of this licence, visit http://creativecommons.org/licenses/by/4.0/.

References

1. Rappaport, T.S.; Sun, S.; Mayzus, R.; Zhao, H.; Azar, Y.; Wang, K.; Wong, G.N.; Schulz, J.K.; Samimi, M.; Gutierrez, F.: Millimeter wave mobile communications for 5G cellular: It will work. IEEE Access **1**, 335–349 (2013). https://doi.org/10.1109/access.2013.2260813
2. Roh, W.; Seol, J.-Y.; Park, J.; Lee, B.; Lee, J.; Kim, Y.; Cho, J.; Cheun, K.; Aryanfar, F.: Millimeter-wave beamforming as an enabling technology for 5G cellular communications: Theoretical

feasibility and prototype results. IEEE Commun. Mag. **52**, 106–113 (2014). https://doi.org/10.1109/mcom.2014.6736750
3. ITU-R. World radio communication conference (WRC-15) final acts. https://www.itu.int/dms_pub/itu-r/opb/act/R-ACT-WRC.12-2015-PDF-E.pdf (2015). Accessed 15 March 2022
4. ITU-R. World radio communication conference (WRC-19) final acts. https://www.itu.int/dms_pub/itu-r/opb/act/R-ACT-WRC.14-2019-PDF-E.pdf (2019). Accessed 15 March 2022
5. Balanis, C.A.: Antenna theory: analysis and design. Wiley, Hoboken (2015)
6. Li, Y.; Luk, K.-M.: Wideband perforated dense dielectric patch antenna array for millimeter-wave applications. IEEE Trans. Antennas Propag. **63**(8), 3780–3786 (2015). https://doi.org/10.1109/tap.2015.2441118
7. Liu, N.W.; Chen, X.P.; Zhu, L.; Liu, Z.X.; Fu, G.: Compact dielectric resonator antenna with bandwidth enhancement via loading of shorting pins. IET Microw. Antennas Propag. **13**(12), 1969–1973 (2019). https://doi.org/10.1049/iet-map.2018.6110
8. Mohsen, M.K.; Isa, M.S.A.M.; Isa, A.A.M.; Abdulhameed, M.K.; Attiah, M.L.; Dinar, A.M.: Enhancement bandwidth of half width-microstrip leaky wave antenna using circular slots. Progr. Electromag. Res. C **94**, 59–74 (2019). https://doi.org/10.2528/pierc19040805
9. Yang, Z.-X.; Yang, H.-C.; Hong, J.-S.; Li, Y.: Bandwidth enhancement of a polarization-reconfigurable patch antenna with stair-slots on the ground. IEEE Antennas Wirel. Propag. Lett. **13**, 579–582 (2014). https://doi.org/10.1109/lawp.2014.2312971
10. Gautam, A.K.; Bisht, A.; Kanaujia, B.K.: A wideband antenna with defected ground plane for WLAN/WiMAX applications. AEU Int. J. Electron. Commun. **70**, 354–358 (2016). https://doi.org/10.1016/j.aeue.2015.12.013
11. Ramanujam, P.; Arumugam, C.; Venkatesan, R.; Ponnusamy, M.: Design of compact patch antenna with enhanced gain and bandwidth for 5G mm-wave applications. IET Microw. Antennas Propag. **14**(12), 1455–1461 (2020). https://doi.org/10.1049/iet-map.2019.0891
12. Li, E.; Li, X.J.; Seet, B.-C.; Lin, X.: Ink-printed flexible wideband dipole array antenna for 5G applications. Phys. Commun. **43**, 101193 (2020). https://doi.org/10.1016/j.phycom.2020.101193
13. Yerlikaya, M.; Gultekin, S.S.; Uzer, D.: A low profile wideband log periodic microstrip antenna design for c-band applications. Adv. Electromag. **8**, 48–52 (2019). https://doi.org/10.7716/aem.v8i2.991
14. Hussain, N.; Azimov, U.; Jeong, M.; Rhee, S.; Lee, S.W.; Kim, N.: A high-gain microstrip patch antenna using multiple dielectric superstrates for WLAN applications. Appl. Comp. Electromag. Soc. J. **35**(2), 187–193 (2020)
15. Das, S.; Sahu, S.: Design of high gain, broadband resonant cavity antenna with meta-material inspired superstrate. AEU-Int. J. Electron. Commun. **100**, 39–46 (2019). https://doi.org/10.1016/j.aeue.2018.12.021
16. Jam, S.; Simruni, M.: Performance enhancement of a compact wideband patch antenna array using EBG structures. AEU-Int. J. Electron. Commun. **89**, 42–55 (2018). https://doi.org/10.1016/j.aeue.2018.03.026
17. de Dieu, N.J.; Sun, L.; Yang, C.; Pang, Y.; Rushingabigwi, G.: Thin-profile wideband and high-gain microstrip patch antenna on a modified AMC. IEEE Antennas Wirel. Propag. Lett. **18**(12), 2518–2522 (2019). https://doi.org/10.1109/lawp.2019.2942056
18. Adibi, S.; Honarvar, M.A.; Lalbakhsh, A.: Gain enhancement of wideband circularly polarized UWB antenna using FSS. Radio Sci. **56**, e2020RS007098 (2021). https://doi.org/10.1029/2020rs007098
19. Peddakrishna, S.; Khan, T.: Performance improvement of slotted elliptical patch antenna using FSS superstrate. Int. J. RF Microw. Comput-Aided Eng. **28**, e21421 (2018). https://doi.org/10.1002/mmce.21421
20. Blanch, S.; Romeu, J.; Corbella, I.: Exact representation of antenna system diversity performance from input parameter description. Electron. Lett. **39**(9), 705–707 (2003). https://doi.org/10.1049/el:20030495
21. Sharawi, M.S.: Printed MIMO antenna engineering. Artech house, Norwood (2014)
22. Sharawi, M.S.: Current misuses and future prospects for printed multiple-input, multiple-output antenna systems. IEEE Antennas Propag. Mag. **59**(2), 162–170 (2017). https://doi.org/10.1109/map.2017.2658346
23. Paulraj, A.J.; Gore, D.A.; Nabar, R.U.; Bolcskei, H.: An overview of MIMO communications-a key to gigabit wireless. Proc. IEEE **92**(2), 198–218 (2004). https://doi.org/10.1109/jproc.2003.821915
24. Jilani, S.F.; Alomainy, A.: Millimeter-wave T-shaped MIMO antenna with defected ground structures for 5G cellular networks. IET Microw. Antennas Propag. **12**(5), 672–677 (2018). https://doi.org/10.1049/iet-map.2017.0467
25. Zhang, Y.; Deng, J.-Y.; Li, M.-J.; Sun, D.; Guo, L.-X.: A MIMO dielectric resonator antenna with improved isolation for 5G mm-wave applications. IEEE Antennas Wirel. Propag. Lett. **18**(4), 747–751 (2019). https://doi.org/10.1109/lawp.2019.2901961
26. Malviya, L.; Parmar, A.; Solanki, D.; Gupta, P.; Malviya, P.: Highly isolated inset-feed 28 GHz MIMO-antenna array for 5G wireless application. Procedia Comput. Sci. **171**, 1286–1292 (2020). https://doi.org/10.1016/j.procs.2020.04.137
27. Hussain, N.; Awan, W.A.; Ali, W.; Naqvi, S.I.; Zaidi, A.; Le, T.T.: Compact wideband patch antenna and its MIMO configuration for 28 GHz applications. AEU-Int. J. Electron. Commun. **132**, 153612 (2021). https://doi.org/10.1016/j.aeue.2021.153612
28. Zahra, H.; Awan, W.A.; Ali, W.A.E.; Hussain, N.; Abbas, S.M.; Mukhopadhyay, S.: A 28 GHz broadband helical inspired end-fire antenna and its MIMO configuration for 5G pattern diversity applications. Electronics **10**(4), 405 (2021). https://doi.org/10.3390/electronics10040405
29. Kamal, M.M.; Yang, S.; Ren, X.-C.; Altaf, A.; Kiani, S.H.; Anjum, M.R.; Iqbal, A.; Asif, M.; Saeed, S.I.: Infinity shell shaped mimo antenna array for mm-wave 5G applications. Electronics **10**(2), 165 (2021). https://doi.org/10.3390/electronics10020165
30. Campbell, C.; Traboulay, I.; Suthers, M.; Kneve, H.: Design of a stripline log-periodic dipole antenna. IEEE Trans. Antennas Propag. **25**, 718–721 (1977). https://doi.org/10.1109/tap.1977.1141653
31. Fernandes, E.M.; da Silva, M.W.; da Silva, B.L.; de Siqueira Campos, A.L.; de Araújo, H.X.; Casella, I.R.; Capovilla, C.E.; Souza, V.P.; de Matos, L.J.: 2.4–5.8 GHz dual-band patch antenna with FSS reflector for radiation parameters enhancement. AEU-Int. J. Electron. Commun. **108**, 235–241 (2019). https://doi.org/10.1016/j.aeue.2019.06.021